

A Search for Seismic Waves from the Impact of the SL/9 R Fragment

CHARLES M. WALTER AND MARK S. MARLEY

Department of Astronomy, Box 30001/Department 4500, New Mexico State University, Las Cruces, New Mexico 88003
E-mail: cwalter@nmsu.edu

DONALD M. HUNTEN,¹ ANN L. SPRAGUE,¹ AND WILLIAM K. WELLS¹

Lunar and Planetary Laboratory, University of Arizona, Tucson, Arizona, 85721

ADITYA DAYAL,¹ WILLIAM F. HOFFMANN,¹ AND MARK V. SYKES

Steward Observatory, University of Arizona, Tucson, Arizona 85721

LYNNE K. DEUTSCH¹

Five College Astronomy Department, University of Massachusetts, Amherst, Massachusetts 01003

GIOVANNI G. FAZIO¹

Optical and Infrared Astronomy Division, Smithsonian Astrophysical Observatory, Cambridge, Massachusetts 02138

AND

JOSEPH L. HORA¹

Institute for Astronomy, University of Hawaii, Honolulu, Hawaii 96822-1839

Received August 1, 1995; revised February 9, 1996

Jupiter was observed in the aftermath of its impact with fragment R of Comet Shoemaker–Levy/9 to search for seismic waves excited by the collision. Observations were made in the 7.8 μm methane emission band with the MIRAC2 camera at the IRTF in an attempt to detect the local perturbation to the equilibrium stratospheric temperature profile induced by the wave. Detection of a jovian seismic wave would provide the tightest constraint to date on interior models of Jupiter. Seismic waves were detected in neither direct images of the planet nor in a composite time–distance diagram which utilizes all of the available imagery. This non-detection allows us to place an upper limit on the energy of the fragment R impact of 1×10^{28} erg, assuming a seismic wave excitation efficiency of 15%. © 1996 Academic Press, Inc.

1. INTRODUCTION

To date our principal probe of the jovian planet interiors has been their gravitational harmonics. The Galileo Probe

¹ Visiting Astronomer at the Infrared Telescope Facility which is operated by the University of Hawaii under contract to the National Aeronautics and Space Administration.

has provided *in situ* measurements, but only of the outermost veneer of Jupiter. Unfortunately, inversion of a planet's gravitational harmonics does not result in a unique interior model. As it has for Earth, only seismology offers the opportunity to uniquely probe the depths of the planet. By detecting waves which have traversed the interior of the planet, seismology can unravel the structure of the deep planetary interior.

A specialized and challenging application of seismology is to measure the normal mode “ringing” of a planet. The frequencies of the normal modes can also be inverted, as is done in helioseismology, to reveal the interior structure. Despite some tantalizing observations, there has yet been no definitive detection of the oscillation modes of any jovian planet (see Deming *et al.* 1989, Schmider *et al.* 1991, Mosser *et al.* 1993, Fisher 1994, and Lederer *et al.* 1995).

The predicted impact and explosion of Comet Shoemaker–Levy/9 into Jupiter offered an unprecedented opportunity to apply the techniques of “classical” geoseismology to the problem of the interior structure of Jupiter. The impact would launch acoustic (or P-) waves that would

traverse the interior of the planet. If these waves could be detected upon their return to the visible atmosphere, a direct and straightforward probe of the interior of Jupiter would be at hand.

Here we report on our attempt to detect primary pressure waves arising from the Shoemaker–Levy/9 fragment R impact from the Infrared Telescope Facility (IRTF). No primary pressure waves were observed, and we provide estimates of the upper limit for the energy of the R impact.

2. THEORY

A variety of waves were predicted to arise from the impacts. Seismic waves were first discussed by Marley (1993, 1994). Deming *et al.* (1994), Gough (1994), Kanamori (1993), Lee and Van Horn 1994, and Lognonné *et al.* (1994) also calculated various properties of impact-induced seismic waves. Hunten *et al.* (1994) presented the observational strategy which we ultimately employed and which is described further below.

The excitation mechanism for the seismic wave is straightforward. As each fragment of the comet enters the atmosphere at 60 km sec^{-1} , it is slowed by its interaction with the atmosphere. Ultimately the comet releases a large fraction of its energy over a short distance, essentially resulting in an explosion (Zahnle and MacLow 1994). From analysis of numerical simulations, MacLow and Zahnle (personal communication) estimated that approximately 15% of the impactor's energy is carried away by a shock wave propagating downward into the planet. This wave decays into an acoustic wave with increasing distance from the explosion. Here, as in Marley (1994), we assume that 15% of the impactor energy is carried away by the wave, independent of the size of the impactor. Zahnle and MacLow (1994) compute a period of between 70 and 140 sec for the wave. Lognonné *et al.* (1994) utilized a seismic moment approach to arrive at a value of 20% for the excitation efficiency and a wave period of 100 sec.

The increase in sound speed with depth in the planet refracts downward-propagating waves back toward the surface. Because the gradient in sound speed with depth near the surface is quite large, the vast majority of the energy in the wave is refracted back upward rapidly and returns to the tropopause near the impact site. Only a small fraction of the energy probes quite deeply into the planet before refracting upward. Our challenge is to detect this modest fraction of the impactor energy, which carries a substantial amount of information about Jupiter's interior.

Marley (1994) presents estimates of both the fraction of the wave energy reaching any given depth in the planet and the arrival times of the returning wave at the tropopause as a function of distance from the impact site. Figure 1 presents the computed arrival times for the seismic wave as a function of distance from the impact site. The wave initially

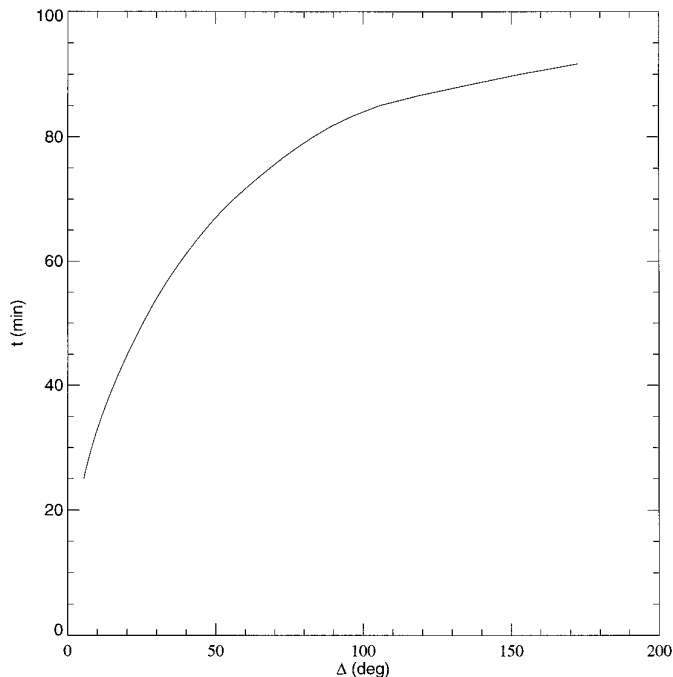


FIG. 1. Predicted angular distance of the seismic wave in degrees (Δ) from the impact site over the time observed. Calculations were done as in Marley (1994) using a Jupiter model of Chabrier *et al.* (1992). This model interpolates over the density discontinuity at the PPT (plasma phase transition). See Lognonné *et al.* (1994) for a more detailed discussion.

traverses the planet very slowly, but after 60 min begins to pick up speed and soon encompasses nearly the diameter of the planet. For this plot the expected wave arrival times were calculated from the Jupiter interior models of Chabrier *et al.* (1992), utilizing an equation of state which interpolated over the likely density discontinuity at the molecular to metallic hydrogen interface. Models with a density interface produce similar results except that a second wave, which reflects from the interface, is also predicted. While we ignore the reflected wave in our analysis below, this has no bearing on the search strategy.

The wave period is almost certainly less than the acoustic cutoff period at the tropopause—about 4 min (Mosser *et al.* 1992). Thus the wave propagates past the tropopause and into the stratosphere. As it traverses the stratosphere it produces the adiabatic temperature fluctuations which we attempted to observe. Marley (1994) utilized a ray tracing or eikonal approach to estimate the temperature amplitude as a function of distance for a given impactor energy. A more sophisticated treatment of wave propagation was presented by Lognonné *et al.* (1994). While such computations would be required to interpret a detected wave, they are not necessary for the wave search and we thus utilize a parameterization derived from the Marley (1994) results below. Nevertheless our predicted temperature amplitudes

are in good agreement with those computed by Lognonné *et al.* for a 10^{27} erg impact (B. Mosser, personal communication).

If the seismic wave period were in fact longer than 4 min the wave would reflect back into the interior near the tropopause, and its amplitude would decay exponentially in the stratosphere making the upper limit derived in Section 4 for the impactor energy too small. We assume throughout this paper that this is not the case.

Since there are no seismometers in place in Jupiter's atmosphere, the observational strategy rests upon detecting the small temperature changes associated with the passing of the wave. This strategy is discussed in detail in Hunten *et al.* (1994). The $7.8 \mu\text{m}$ methane band was chosen because of two advantageous properties. While the majority of emission seen in the mid-IR from Jupiter is formed near the tropopause at ~ 100 mbar, the ν_4 band of methane is particularly strong. Thus emission in this band arises from higher levels in the atmosphere. The weighting function for our bandpass peaks in the stratosphere at $P \sim 20$ mbar (Orton 1977). Since the temperature fluctuation produced by a propagating pressure wave is inversely proportional to the square root of the atmospheric density, it is better to search higher in the atmosphere for a given wave, all else being equal.

Furthermore in Jupiter's stratosphere this band lies on the Wien side of the peak in the Planck function. Differentiating the logarithm of the Planck function with respect to the logarithm of the temperature gives a relationship solely dependent on the frequency ν and the temperature T ,

$$\frac{d \ln B}{d \ln T} = \frac{x}{1 - e^{-x}} \approx x, \quad (1)$$

for $x \gg 1$ where $x = h\nu/kT$. As a result, slight temperature perturbations produce substantially larger flux variations. For conditions in the upper stratosphere $B \propto T^{12}$, and a temperature fluctuation of just 1 K (or 0.68%) increases the radiance by 8.5%.

A drawback to working in a relatively narrow bandpass is that the absolute flux is low, requiring comparatively long integration times to obtain images with acceptable S/N. The $7.8 \mu\text{m}$ band also sits on the shoulder of a telluric water vapor band and is thus subject to the concomitant variations in terrestrial atmosphere opacity. Mosser *et al.* (1996) thus chose to observe at a longer wavelength, sacrificing sensitivity to the stratosphere for higher S/N images.

The weighting function to the emergent flux from Jupiter in our $7.8 \mu\text{m}$ bandpass (Orton 1977) constrains our wave period sensitivity. This function peaks at 20 mbar, with its full vertical extent at half maximum of the peak being approximately 35 km. At 20 mbar the nominal seismic wave has a period of 120 sec, a wavelength of 110 km,

and takes about 40 sec to traverse the weighting function. Requiring that no more than one half wavelength of the acoustic wave lies within the weighting function conservatively places our detection cutoff at 80 sec. We are not sensitive to shorter period waves.

During an exposure of 1.9 sec, the wave does not move appreciably through the detection region. Thus positive and negative vertical temperature fluctuations arising from wave propagation during the exposure are not a concern. Furthermore, the frame rate of about 1 image/10 sec is sufficient to resolve the passage of the wave through the weighting function. The horizontal appearance of the wave also limits our sensitivity, as various wavefronts arrive at slightly different times in adjoining regions of atmosphere. We consider this issue fully in Section 4.

3. OBSERVATIONS

Observations were made at the 3-m IRTF on Mauna Kea, Hawaii, on July 21, 1994 UT. We imaged Jupiter's thermal emission with MIRAC2 (Hoffmann *et al.* 1993, 1994). MIRAC2 is a mid-infrared array camera which utilizes a Rockwell HF16 128×128 Si:As hybrid BIB array. Reflective optics in the camera liquid-helium cryostat produce images at a nominal scale of $0.34''/\text{pixel}$, allowing it to be one of the first cameras to image the entire disk of Jupiter in the thermal IR. The effective spectral range of the camera is $2.2\text{--}25 \mu\text{m}$. Even though the IRTF was dedicated during the month surrounding the impacts to observations of the comet and Jupiter (Orton *et al.* 1995), seismic waves were only searched for in the aftermath of the R impact due to poor weather conditions.

We observed for 80 min following the impact (5:41 UT—Hammel *et al.* 1995). Using a CVF filter centered at $7.85 \mu\text{m}$ with a 1.8% bandpass we obtained 214 images typically separated by 10 sec, each with an 1.97 sec exposure time. Images of the star Alpha Boo taken prior to impact and of Callisto taken 90 min following impact both yield a point spread function with a Gaussian FWHM of $0.9''$.

The data was obtained in grab-nod mode with a frame time of 32.8 msec. Sixty frames were acquired on the target and coadded for an exposure of 1.97 sec. Then the telescope was nodded slightly off-target to obtain a similar 60 sky frames. Thus each coadded Jupiter image had an associated sky image that was subtracted in the reduction process. A nearest neighbor algorithm was used to correct for the typically 10 bad pixels per image. This technique was also used in 75 images in which a camera channel malfunctioned, making 1 of every 16 pixels unreliable. By cross-correlating each image with a simulated oblate jovian disk, we were able to center all images to within 0.5 pixel. The resulting images have a typical signal-to-noise ratio of 5 per pixel as measured from the average pixel value and

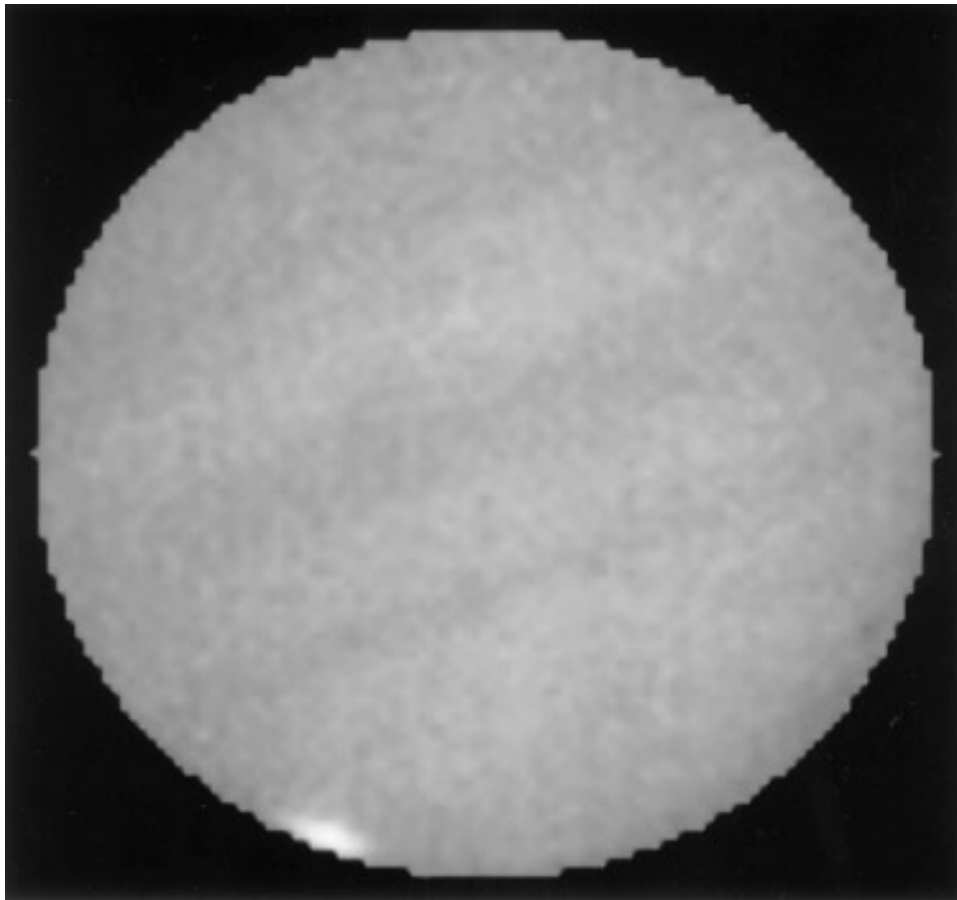


FIG. 2. A typical image from our data set. This image was taken at 6:04:52 UT on 21 July 1994 and has been sky and bias-subtracted, corrected for bad pixels, centered, and had the background removed.

associated variances in a ring 3 pixels wide centered 40° from the image center (see Fig. 2 for a typical image).

4. ANALYSIS

Prior to analysis the images were corrected for bias and scaled to have identical mean fluxes in the central 5% of the planet. This normalization was necessary to correct for the extremely variable transmission arising from small-scale atmospheric fluctuations. After normalization, the integrated planetary flux (excluding the impact site) was found to vary by no more than 1% in the 80 min observing window. Passage of the seismic wave through the normalization region does not occur until near the end of the observing window when the wave perturbation would be undetectable. No other atmospheric structures which might affect the normalization are present in the images. In any case, detection of the wave requires only relative photometry.

Three jovian zonal features are visible in all images. These were removed by dividing each image by a compos-

ite image constructed by coadding the entire dataset. Since the only structure visible below -30° latitude was the impact site itself, the composite image was smoothed to a mean value determined from the rest of the planet in this region, in effect not performing a correction there. Thus the impact site remains visible in the final images.

The reduced images showed no immediate signature of the seismic wave. We made several attempts to detect waves by coadding all images taken within various windows, up to 3 min. In no case was a wave detected. To extend the analysis required the use of a technique which incorporated the entire dataset.

Since we are most interested in the arrival time of the seismic wave back into the observed atmosphere of Jupiter, and not its detailed shape, we constructed a time–distance diagram, as first suggested by Mosser *et al.* (1995) who refer to this plot as a “hodogram.” In this analysis, each pixel from every image of Jupiter is reprojected onto a single image in which the horizontal axis is the angular separation of the pixel from the impact site and the vertical axis is the time elapsed since impact. Individual images

thus collapse into a single horizontal line in the plot where the pixel brightness along the line denotes the average brightness value of all pixels a given angular distance from the impact site. Images taken at different times fill out the plot vertically.

The first step of this analysis was to map each pixel on the disk to a planetocentric coordinate. We used algorithms modified from the program AMIE (Hockey and Barnet 1994), which is an update of software developed at JPL to navigate Voyager data (Jepsen *et al.* 1980). We modified the code to allow for the reprojection of planetary images from composite mosaics. This software takes the 6% oblateness and camera scale into account when mapping each pixel, and then uses the relevant pixel and impact point coordinates to determine the angular distance Θ using spherical trigonometry with θ representing the latitude and ϕ the longitude,

$$\cos \Theta = \sin \theta_1 \sin \theta_2 + \cos \theta_1 \cos \theta_2 \cos(\phi_1 - \phi_2). \quad (2)$$

For the location of the impact site we used the results of Hammel *et al.* (1995). Assuming the expanding transient ring feature observed in HST images originated at the impact site they solved for the center of the ring, accounting for the oblateness of the planet. Averaging the results of three images yielded an impact point located at $-44.17 \pm 0.1^\circ$ planetocentric latitude and $46.8 \pm 0.5^\circ$ System III longitude. This was then propagated throughout the analysis assuming a System III rotational period of 9.92492 hr (presumably appropriate for a wave traveling through the deep interior).

This approach offers two advantages. By azimuthally averaging over all pixels where the returning wave produces a signal at a given instant, we increase the S/N ratio by approximately the square root of the number added. This typically improved the S/N per pixel in the time–distance diagram to ~ 100 . A seismic wave would appear as a curve across the time–distance diagram since the wave moves in both azimuth and time, while fixed features appear as a vertical stripe since they co-rotate with the impact point. Figure 3 shows the resultant time–distance diagram for our dataset. Each pixel is 0.5° wide and 10 sec tall (the typical time between images). Horizontal black stripes represent times during which no images were taken.

The large, bright regions of heated atmosphere arising from the hyper-velocity re-entry of ejecta material swamp any waves near the impact site (Graham *et al.* 1994). These areas effectively prevent the detection of waves during the first 30 min following the impact. No wave is detected in the remainder time–distance diagram. Other diagrams were constructed employing a running 3 min window of summed images. Again, no wave signature was found. We thus next attempted to place an upper limit on the impact size.

To test the sensitivity of our time–distance diagram, we added a variety of simulated waves arising from varying impact energies. The predicted temperature amplitudes and wave locations were computed following Marley (1994). Note that the temperature amplitudes in the published version of his Fig. 3 are incorrect, although correct values are derived in the text and used in our calculation.

In those images taken from 30–80 min after impact, we added an artificial wave feature computed at 10 sec intervals to the individual images before azimuthal averaging. Utilizing Eq. (1), we converted temperature perturbations to flux perturbations. The flux perturbation for each pixel was computed by assuming a sinusoidal temperature variation over the projected wavelength as computed by Hunten *et al.* (1994). They found that

$$W = \frac{c \Delta t}{\sin \theta_0}, \quad (3)$$

where W is the width of the wavefront, c the appropriate speed of sound (0.89 km sec^{-1} at 20 mbar), Δt the wave period (we assume 120 sec), and θ_0 the takeoff angle of the relevant portion of the wavefront. We then decomposed the projected wavelength into 32 separate regions, each receiving the appropriate temperature perturbation as shown in Fig. 4. The contribution from both the wave compression as well as from the following rarefaction are included. We assume the maximum temperature perturbation appears in the first wavelength and neglect subsequent waves. The total flux variation was then projected onto individual pixels, accounting for the ratio of the wavefront width to the pixel size as in Fig. 4. The final artificial wave is then convolved with a Gaussian FWHM of $0.9''$ (2.4 pixels) and added to the image.

The resulting relative flux ratios, $\delta F/F$, where F is the unperturbed pixel flux, are displayed in Fig. 5. In this figure the wave is constructed and added to our dataset as above. The perturbation is then plotted as a percentage variance from the background level over the relevant portion of the observing window. Before the impacts, Deming (1994) computed the expected relative flux perturbation as a function of distance for the impact point. His computations were for a 6×10^{29} erg impact observed by diffraction-limited telescopes of various apertures. To compare the two models, it is necessary to quantify the “effective” diffraction-limited aperture of our telescope. Our FWHM implies a 2.2-m telescope, however the smearing response of the system with respect to the core of the PSF equals that of a telescope 2 times smaller. When that is taken into consideration, our computations of $\delta F/F$ agree well with Deming’s predicted performance from 55 to 80 min following the impact.

An example of a resultant time–distance diagram with a clearly delineated wave signature is shown in Fig. 6. This

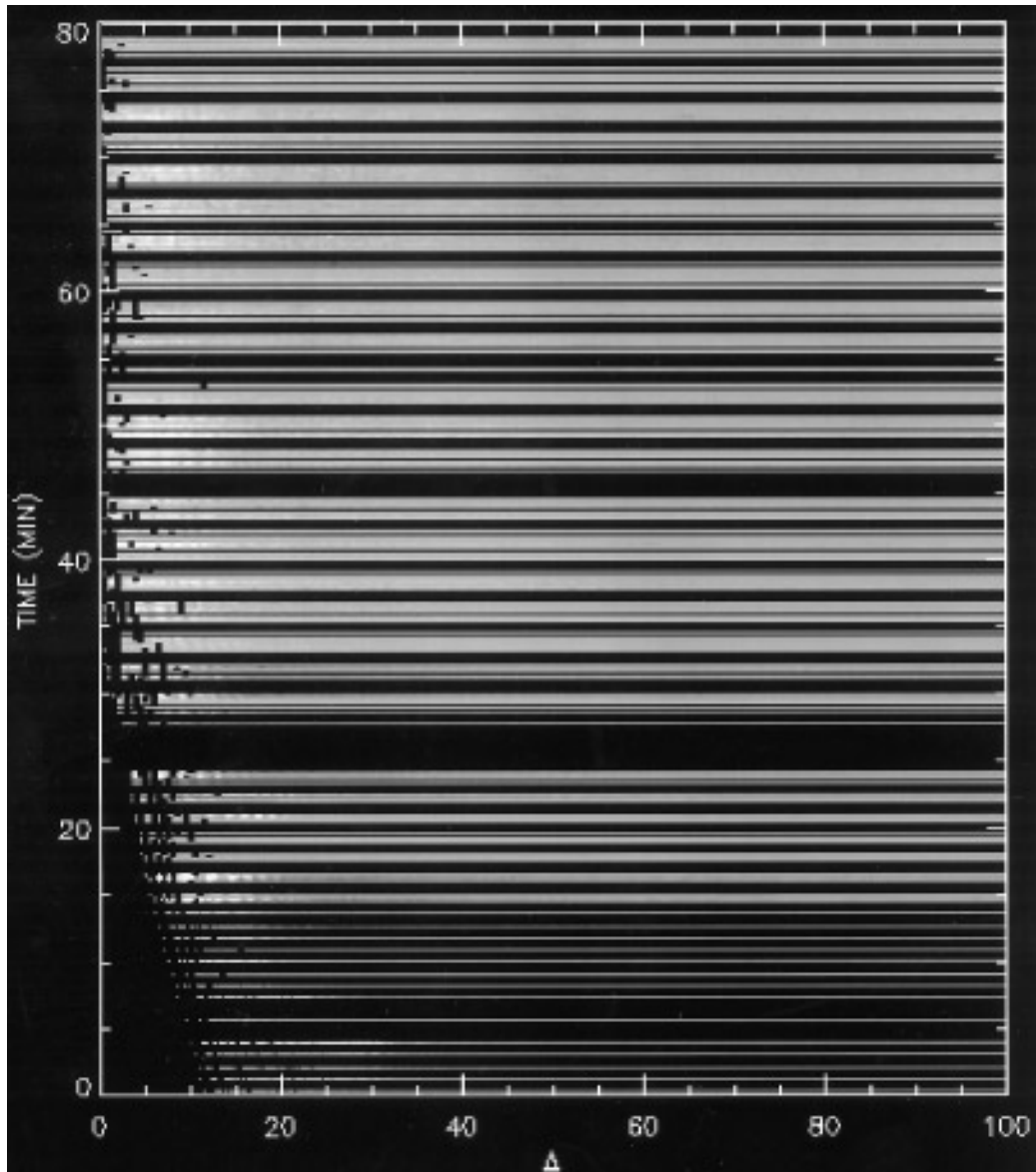


FIG. 3. A time–distance diagram representing the 80 min of data following the impact. Pixels are 0.5° by 10 sec (the typical time between images). The relative intensity is shown as a function of distance in degrees (Δ) from the impact site over time. There is evidence from 19–28 min of greater emission from the still-heated impact point, but no evidence for a seismic wave is visible. The time–distance diagram is discussed further in section 4.

signature is detectable down to impact energies of 1×10^{28} erg. The wave signature is clearest between 40 and 60 min following the impact, when the wave has moved far enough beyond the heated impact region and encompasses enough pixels on the planet that when azimuthally averaged, it stands out above the noise. At later times the temperature amplitude is too small to be detected.

Note that on a spherical planet the returning wavefront would appear to spread out from the impact point in the form of a coherent ring. This is the feature searched for in the time–distance analysis. Jupiter, however, is oblate.

Thus waves leaving the impact point at a given takeoff angle from the vertical but propagating into different azimuths return to the tropopause at different times since they must travel different path lengths. A full treatment of this problem requires following the wave propagation through oblate level surfaces computed from a jovian interior model that accounts for rotation. A perturbation analysis to first order in oblateness reveals that the departure of the returning wave front from a circle projected onto the planet does not exceed 1° at any azimuth until 60 min after impact. The error is less than the projected seeing

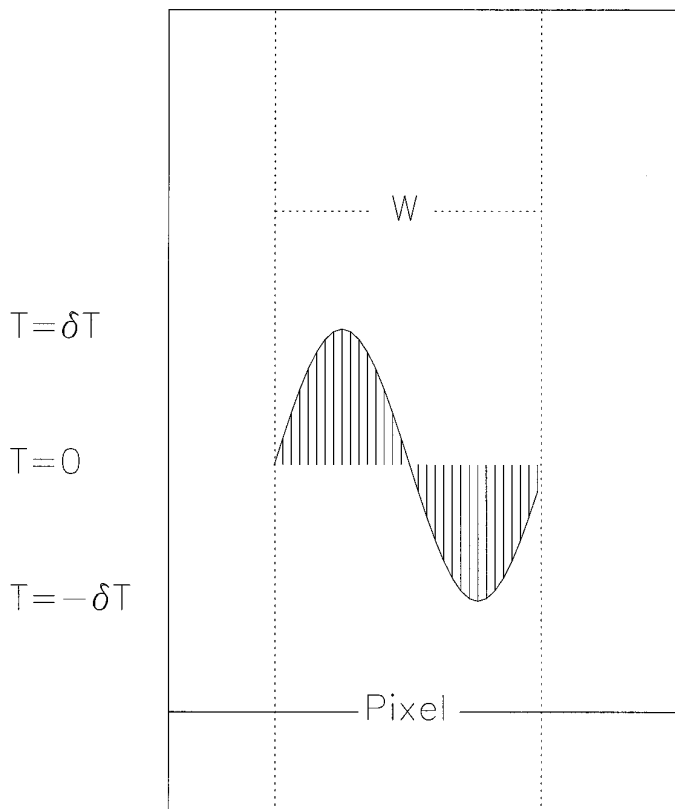


FIG. 4. Diagram illustrating how the artificial seismic wave was added to the data to derive the impact energy upper limit. The wavefront location and width are determined at the time corresponding to every image. The wavefront, as seen from above (Hunten *et al.* 1994), is then divided into 32 partitions for which a temperature perturbation δT and a flux perturbation is calculated. The total flux perturbations over the wavelength is then summed and scaled to the width of the pixel.

disk for all times less than 70 min after impact. Since the detection limit is controlled by observations at times less than 50 min, neglect of the oblateness of the planet does not affect our derived impact energy limit. Were a wave detected, a more complex analysis would be required to follow the wave at $t > 70$ min.

5. DISCUSSION

It is interesting to compare the impact energy limit derived from the seismic wave analysis for the R impact with other impact energy estimates. Given a spherical comet fragment with a density of 1 g cm^{-3} impacting the planet at 60 km sec^{-1} , a 10^{28} erg energy limit yields a maximum diameter for the R fragment of 1.0 km.

A group led by Benoit Mosser (Mosser *et al.* 1996) also searched for seismic waves in the aftermath of impacts A, H, and L. The largest impact observed by this group was of fragment L, which they observed from the Nordic Optical Telescope at $10 \mu\text{m}$. While this group has many more

images with substantially better signal-to-noise (Mosser *et al.* 1996), emission at $10 \mu\text{m}$ is formed much deeper in the atmosphere and is correspondingly less sensitive to wave perturbations. Their detection limit for the L impact (Mosser *et al.* 1995) is 5×10^{27} erg, or a fragment smaller than 0.81 km in diameter, assuming 20% wave excitation efficiency.

Hammel *et al.* (1995) grouped the impact sites into classes based on the size of the dark ejecta and the number of visible waves. Fragment L was considered to be one of the largest and was placed in class 1. Following behind in class 2a were fragments A and H, and fragment R fell into class 2b. The seismic wave constraints on impact energies are consistent with this classification. Given that the L impact apparently produced some of the greatest effects, it is useful to consider the Mosser *et al.* result for the L impact as an effective upper limit for the energy of all the impacts.

From HST observations of the nucleus, Weaver *et al.* (1995) estimated a diameter for fragment R of 2.5 km. This exceeds our upper limit if the object is fully dense ice. Graham *et al.* observed the R splash at $2.3 \mu\text{m}$ from the Keck Telescope on Mauna Kea. By integrating over the lightcurve they placed a lower limit for the impact energy

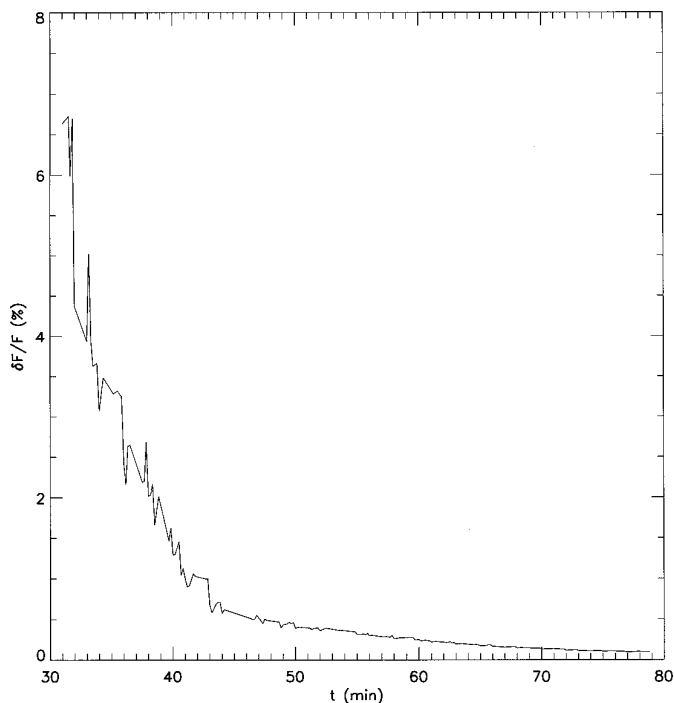


FIG. 5. As in Deming (1994) the effect of a theoretical seismic wave from an impact of energy 6×10^{29} erg has been convolved with our PSF. The figure shows the result of adding this artificial wave to our data set. The corresponding ratio of the peak perturbation to the background is shown as a function of time. The jaggedness between 30 and 45 min arises from poor wave resolution attributable to the heated impact region.

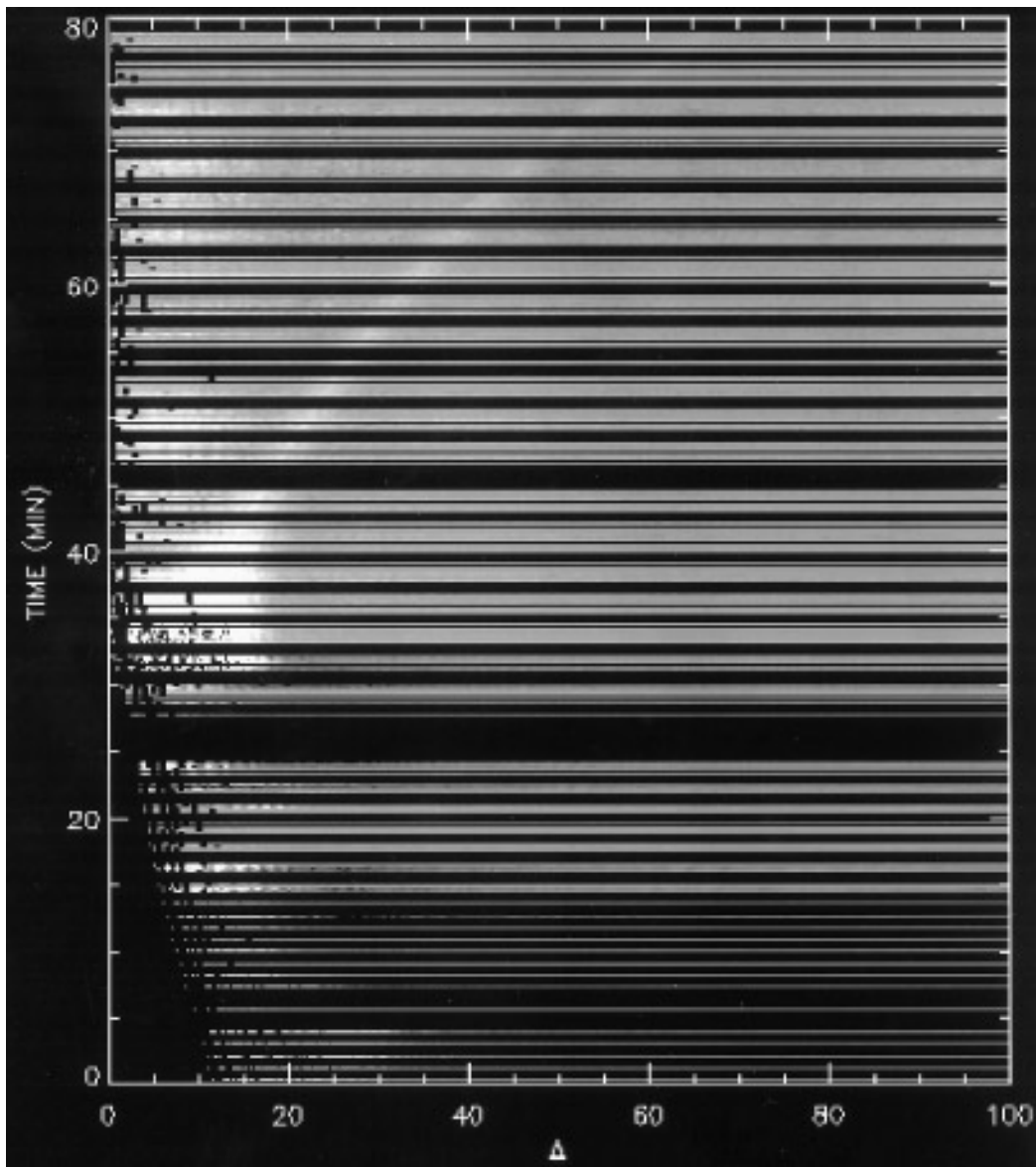


FIG. 6. This time–distance diagram is identical to Fig. 3 except for the addition of an artificial wave. The wave signature is identifiable as a curve originating at 14° and 40 min.

of 3×10^{24} erg, or a fragment diameter of 0.07 km. Zahnle and MacLow (1995) can best model the R lightcurves from 2.3 to $4.5 \mu\text{m}$ with an impact energy of 6×10^{26} erg.

Our primary uncertainty in estimating the impactor energy is poor knowledge of the wave excitation efficiency and wave period. The wave characteristics of Zahnle and MacLow (1994) are based upon limited numerical experiments. Lower excitation efficiencies would result in a larger upper limit and vice versa. The role played by the wave period is slightly more complex, as it factors into the predicted temperature amplitudes in two separate manners. First the wave flux is inversely proportional to the period (Marley 1994, Eq. (2)) so the temperature perturbation

$\delta T \propto \Delta t^{-1/2}$. However the width of the wavefront and thus the intensity of the measurable disturbance varies directly as the wave period (Eq. (2)). These two factors make the observed flux proportional to $\Delta t^{1/2}$. A more robust estimate of these parameters would strengthen the impact energy limits set by the seismological studies.

6. CONCLUSIONS

We attempted to detect a seismic signature in the aftermath of the impact of the SL/9 R fragment. No seismic waves were detected in either direct imaging or in a travel time diagram. Such a detection would have opened a sub-

stantial new window into the interiors of the jovian planets. Seismology has, however, allowed us to place an upper limit to the R impact energy of 1×10^{28} erg. This limit is consistent with some other observations, but is smaller than that found by Weaver *et al.* (1995), if the comet is fully dense ice. Assuming this composition, our upper limit to the fragment diameter is 1 km.

These results also demonstrate the substantial promise for planetary seismology offered by the $7.8 \mu\text{m}$ methane band and infrared array detectors capable of imaging the entire planet. MIRAC2 was also employed after the impact period to search for global oscillation modes of Jupiter excited by the impacts. Results of this search will be reported elsewhere.

ACKNOWLEDGMENTS

The authors thank Benoit Mosser and an anonymous referee for insightful reviews. We also thank Mordecai Mark MacLow and Kevin Zahnle for helpful discussions and shocking results from their numerical models. The MIRAC camera upgrade to the 128×128 array was supported by Steward Observatory of the University of Arizona, the Smithsonian Astrophysical Observatory, the National Science Foundation, and the National Aeronautics and Space Administration.

REFERENCES

- CHABRIER, G., D. SAUMON, W. B. HUBBARD, AND J. I. LUNINE 1992. The molecular-metallic transition of hydrogen and the structure of Jupiter and Saturn. *Astrophys. J.* **391**, 817–826.
- DEMING, D., M. J. MUMMA, F. ESPENAK, D. E. JENNINGS, T. KOSTIUK, G. WIEDEMANN, R. LOEWENSTEIN, AND J. PISCITELLI 1989. A search for p-mode oscillations of Jupiter; Serendipitous observations of non-acoustic thermal wave structure. *Astrophys. J.* **343**, 456–467.
- DEMING, D. 1994. Prospects for jovian seismological observations following the impact of Comet Shoemaker–Levy 9. *Geophys. Res. Lett.* **21**, 1095–1098.
- FISHER, B. 1994. *High Time-Resolution Infrared Imaging Observations of Jupiter*. PhD. Thesis, University of California, San Diego.
- GOUGH, D. O. 1994. Seismic consequences of the Shoemaker–Levy impact. *Mon. Not. R. Astron. Soc.* **269**, L17–L20.
- GRAHAM, J. R., I. DE PATER, J. G. JERNIGAN, M. C. LIU, AND M. E. BROWN 1995. The fragment R collision: W. M. Keck Telescope observations of SL9. *Science* **267**, 1320–1323.
- HAMMEL, H. B., R. F. BEEBE, A. P. INGERSOLL, G. S. ORTON, J. R. MILLS, A. A. SIMON, P. CHODAS, J. T. CLARKE, E. DE JONG, T. E. DOWLING, J. HARRINGTON, L. F. HUBER, E. KARKOSCHKA, C. M. SANTORI, A. TOIGO, D. YEOMANS, AND R. A. WEST 1995. HST imaging of atmospheric phenomena created by the impact of Comet Shoemaker–Levy 9. *Science* **267**, 1288–1295.
- HOCKEY, T. AND C. BARNET 1994. A DOS-based version of the VICAR image processing system for planetary image reduction, navigation, and measuring. *Bull. Am. Astron. Soc.* **26**, 184.
- HOFFMANN, W. F., G. G. FAZIO, K. SHIVANANDAN, J. L. HORA, AND L. K. DEUTSCH 1993. MIRAC, a mid infrared array camera for astronomy. *Proc. SPIE* **1946**, 449–460.
- HOFFMANN, W. F., G. G. FAZIO, K. SHIVANANDAN, J. L. HORA, AND L. K. DEUTSCH 1994. Astronomical observations with the mid-infrared array camera, MIRAC. *Infrared Phys. Technol.* **35**, 175–194.
- HUNTEN, D. M., W. F. HOFFMANN, AND A. L. SPRAGUE 1994. Jovian seismic waves and their detection. *Geophys. Res. Lett.* **21**, 1091–1094.
- JEPSEN, A. L., J. A. MOSHER, G. M. YAGI, C. C. AVIS, J. J. LORRE, AND G. W. GARNEAU 1980. Voyager image processing at the Image Processing Laboratory. *J. Br. Interplanet. Soc.* **33**, 315–322.
- KANAMORI, H. 1993. Excitation of jovian normal modes by an impact source. *Geophys. Res. Lett.* **20**, 2921–2924.
- LEDERER, S. M., M. S. MARLEY, B. MOSSER, J. P. MAILLARD, N. J. CHANOVER, AND R. F. BEEBE 1995. Albedo features and jovian seismology. *Icarus* **114**, 269–277.
- LEE, U., AND H. M. VAN HORN 1994. Global oscillation amplitudes excited by the Jupiter–comet collision. *Astrophys. J.* **405**, 359–374.
- LOGNONNÉ, P., B. MOSSER, AND F. DAHLEN 1994. Excitation of jovian seismic waves by the Shoemaker–Levy/9 impact. *Icarus* **110**, 180–195.
- MARLEY, M. S. 1993. The seismological impact of Comet Shoemaker–Levy. *Bull. Am. Astron. Soc.* **25**, 1043.
- MARLEY, M. S. 1994. Seismological consequences of the collision of Comet Shoemaker–Levy/9 with Jupiter. *Astrophys. J.* **427**, L63–L66.
- MOSSER, B., D. GAUTIER, AND T. KOSTIUK 1992. On the detectability of jovian oscillations with infrared heterodyne measurements. *Icarus* **96**, 15–26.
- MOSSER, B., D. MÉKARNIA, J. P. MAILLARD, J. GAY, D. GAUTIER, AND P. DELACHE 1993. Seismological observations with a Fourier transform spectrometer: Detection of jovian oscillations. *Astron. Astrophys.* **267**, 604–622.
- MOSSER, B., P. GALDEMARD, R. JOUAN, P. LAGAGE, E. PANTIN, M. SAUVAGE, P. LOGNONNÉ, D. GAUTIER, P. DROSSART, P. MERLIN, F. SIBILLE, I. VAUGHLIN, F. BILLEBAUD, T. LIVENGOOD, H. U. KÄUFL, M. MARLEY, M. HULTDGREN, L. NORDH, G. OLOFSSON, A. ULLA, J. A. BELMONTE, C. REGULO, T. ROCA-CORTES, M. SELBY, J. M. RODRIGUEZ ESPINOSA, AND I. VIDAL 1995. Seismic studies of Jupiter at the time of the SL-9 impacts. In *European SL-9/Jupiter Workshop, Garching, 13–15 February 1995* (R. M. West and H. Boehnhardt, Eds.), European Southern Observatory Conference and Workshop Proceedings 52, pp. 397–402. ESO, Garching.
- MOSSER, B., P. GALDEMARD, P. LAGAGE, E. PANTIN, M. SAUVAGE, P. LOGNONNÉ, D. GAUTIER, F. BILLEBAUD, T. LIVENGOOD, AND H. U. KÄUFL 1996. Impact seismology: A search for primary pressure waves following impacts A and H. *Icarus* **121**, 331–340.
- ORTON, G. S. 1977. Recovery of the mean jovian temperature structure from inversion of spectrally resolved thermal radiance data. *Icarus* **32**, 41–57.
- ORTON, G., M. A'HEARN, K. BAINES, D. DEMING, T. DOWLING, J. GOGUEN, C. GRIFFITH, H. HAMMEL, W. HOFFMANN, D. HUNTEN, D. JEWITT, T. KOSTIUK, S. MILLER, K. NOLL, K. ZAHNLE, N. ACHILLEOS, A. DAYAL, L. DEUTSCH, F. ESPENAK, P. ESTERLE, J. FRIEDSON, K. FAST, J. HARRINGTON, J. HORA, R. JOSEPH, D. KELLY, R. KNACKE, J. LACY, C. LISSE, J. RAYNER, A. SPRAGUE, M. SHURE, K. WELLS, P. YANAMANDRA-FISHER, D. ZIPOY, G. BJORAKER, D. BUHL, W. GOLISCH, D. GRIEP, C. KAMINSKI, C. ARDEN, A. CHAIKIN, J. GOLDSTEIN, D. GILMORE, G. FAZIO, T. KANAMORI, H. LAM, T. LIVENGOOD, M.-M. MACLOW, M. MARLEY, T. MOMARY, D. ROBERTSON, P. ROMANI, J. SPITALE, M. SYKES, J. TENNYSON, D. WELLNITZ, AND S.-W. YING 1995. Collision of Comet Shoemaker–Levy 9 with Jupiter observed by the NASA Infrared Telescope Facility. *Science* **267**, 1277–1282.

- SCHMIDER, F.-X., B. MOSSER, AND E. FOSSAT 1991. A possible detection of jovian global oscillations. *Astron. Astrophys.* **248**, 281–291.
- WEAVER, H. A., M. F. A'HEARN, C. ARPIGNY, D. C. BOICE, P. D. FELDMAN, S. M. LARSON, P. LAMY, D. H. LEVY, B. G. MARSDEN, K. J. MEECH, K. S. NOLL, J. V. SCOTTI, Z. SEKANINA, C. S. SHOEMAKER, E. M. SHOEMAKER, T. E. SMITH, S. A. STERN, A. D. STORRS, J. T. TRAUGER, D. K. YEOMANS, B. ZELLNER 1995. The Hubble Space Telescope (HST) observing campaign on Comet Shoemaker–Levy 9. *Science* **267**, 1282–1287.
- ZAHNLE, K. AND M.-M. MACLOW 1994. The collision of Jupiter and Comet Shoemaker–Levy9. *Icarus* **108**, 1–18.
- ZAHNLE, K., AND M.-M. MACLOW 1995. A simple model for the light curve generated by a Shoemaker–Levy 9 impact. *J. Geophys. Res. Planets* **100**, 16,885–16,894.